



**HAL**  
open science

## 3D analysis of the osteonal and interstitial tissue in human radii cortical bone

Rémy Gauthier, Helene Follet, Cécile Olivier, David Mitton, Françoise Peyrin

► **To cite this version:**

Rémy Gauthier, Helene Follet, Cécile Olivier, David Mitton, Françoise Peyrin. 3D analysis of the osteonal and interstitial tissue in human radii cortical bone. *BONE*, 2019, 127, pp.526-536. 10.1016/j.bone.2019.07.028 . hal-02304636

**HAL Id: hal-02304636**

**<https://hal.science/hal-02304636>**

Submitted on 19 Dec 2019

**HAL** is a multi-disciplinary open access archive for the deposit and dissemination of scientific research documents, whether they are published or not. The documents may come from teaching and research institutions in France or abroad, or from public or private research centers.

L'archive ouverte pluridisciplinaire **HAL**, est destinée au dépôt et à la diffusion de documents scientifiques de niveau recherche, publiés ou non, émanant des établissements d'enseignement et de recherche français ou étrangers, des laboratoires publics ou privés.

# 3D analysis of the osteonal and interstitial tissue in human radii cortical bone

---

Rémy Gauthier<sup>1,2</sup>, Hélène Follet<sup>3</sup>, Cécile Olivier<sup>2</sup>, David Mitton<sup>1</sup> and Françoise Peyrin<sup>2,\*</sup>

<sup>1</sup> Univ Lyon, Université Claude Bernard Lyon 1, IFSTTAR, LBMC UMR\_T9406, F69622, Lyon, France;

<sup>2</sup> Univ Lyon, CNRS UMR 5220, Inserm U1206, INSA Lyon, Université Claude Bernard Lyon 1, Creatis, F69621 Villeurbanne Cedex, France;

<sup>3</sup> Univ Lyon, Université Claude Bernard Lyon 1, INSERM, LYOS UMR1033, F69008, Lyon, France ;

10

11 \* Corresponding author: [peyrin@esrf.fr](mailto:peyrin@esrf.fr)

## 12 Abstract:

13 Human cortical bone has a complex hierarchical structure that is periodically remodelled throughout  
14 a lifetime. This microstructure dictates the mechanical response of the tissue under a critical load. If  
15 only some structural features, such as the different porosities observed in bone, are primarily studied,  
16 then investigations may not fully consider the osteonal systems in three-dimensions (3D). Currently, it  
17 is difficult to differentiate osteons from interstitial tissue using standard 3D characterization methods.  
18 Synchrotron radiation micro-computed tomography (SR- $\mu$ CT) in the phase contrast mode is a  
19 promising method for the investigation of osteons. In the current study, SR- $\mu$ CT imaging was  
20 performed on cortical bone samples harvested from eight human radii (female, 50-91 y.o.). The images  
21 were segmented to identify Haversian canals, osteocyte lacunae, micro-cracks, as well as osteons. The  
22 significant correlation between osteonal and Haversian canal volume fraction highlights the role of the  
23 canals as sites where bone remodelling is initiated. The results showed that osteocyte lacunae  
24 morphometric parameters depend on their distance to cement lines, strongly suggesting the evolution  
25 of biological activity from the beginning to the end of the remodelling process. Thus, the current study  
26 provides new data on 3D osteonal morphometric parameters and their relationships with other  
27 structural features in humans.

28 **Keyword:** Human cortical bone, synchrotron radiation, micro-computed tomography, osteons,  
29 cement lines, osteocytes lacunae

## 30 1. Introduction

31 Bone fragility generated by diseases such as osteoporosis is known to be associated with structural  
32 changes in the tissue [1].

33 The difficulty in predicting such increases in fragility is mainly due to the highly complex organization  
34 of the tissue. Bone structure is made up of different features observed at different length scales, from  
35 the collagen fibril up to the osteonal system, which includes osteocyte lacunae and vascular canals [1–  
36 4]. All of these length scales are assumed to be involved in cortical bone crack propagation mechanisms  
37 such as micro-cracking or crack deflection [5–10]. However, despite several qualitative observations  
38 regarding the implication of osteons in the crack deflection mechanism [11,12], only a few studies

39 provide quantitative 3D data due to the difficulty in quantifying their morphometric properties  
40 [9,13,14].

41 Osteonal areas arise in cortical bone through a remodelling process at the surface of osteonal canals  
42 [15–18], and as such, they surround these canals. The remodelling process consists of the formation  
43 of young tissue to replace older, damaged tissue through cellular mechanisms [19,20]. As  
44 mineralization increases with time [21–23], new remodelled tissue is less mineralized than older tissue.  
45 As such, the osteon is different from its surrounding tissue, referred to as interstitial tissue. The  
46 osteonal and interstitial tissues are separated by an interface called the cement line (CL), which is  
47 assumed to have a specific mineralization [24–27]. In reality, the area of cortical bone called interstitial  
48 tissue is composed of fragments of older osteons in which mineralization has highly increased with  
49 time [28]. This mixture of different fragments of osteons made them no more distinguishable between  
50 each other, thus random organization is observed. It has been suggested that osteocyte lacunae may  
51 have different properties within the osteon according to their distance to this CL [29–31]. Similarly,  
52 there are different types of lamellae that exist with different structural and mechanical properties  
53 [29,32–37]. This finding strongly suggests the evolution of biological activity during osteon formation  
54 and maturation of the tissue through mineralization.

55 Despite the differences in mineralization in the osteon compared to interstitial tissue, it is still difficult  
56 to identify osteons using standard characterization methods. In previous studies, analysis of osteons  
57 was mainly done manually using micro-radiography [38–40], histology [14,41], polarized light  
58 microscopy [42], or electron microscopy [13]. These techniques provide 2D data of the osteonal system  
59 ; however, bone has a complex 3D architecture [4,43,44].

60 Absorption Synchrotron Radiation Micro-Computed Tomography (SR- $\mu$ CT) images allow for the  
61 visualization of contrast in osteons. To further segment osteons, a dedicated segmentation method  
62 had been proposed [45]. Hannah et al. also segmented osteons through 3D SR- $\mu$ CT by averaging  
63 tomographic slices over 835  $\mu$ m in order to enhance the sensitivity to density variations [30]. However,  
64 this method provides osteonal features that have the same geometry over 835  $\mu$ m, which may not be  
65 representative of reality. In 2011, Cooper et al. showed that the phase contrast enhancement mode in  
66 3D SR- $\mu$ CT could be beneficial to the segmentation of osteons [46]. By placing the samples at some  
67 distance from the detector, one can enhance the edges around the borders of osteons. However, in  
68 their study, Cooper et al. only investigated the femoral diaphysis of a unique human donor, thus  
69 providing a good feasibility study, but insufficient data for quantitative analysis. Use both the phase  
70 contrast enhancement mode and quantitative phase retrieval improves contrast of osteons [11,25].  
71 Nevertheless, despite increasing contrast, automatic segmentation of osteons remains challenging and  
72 there is currently very little 3D quantitative data.

73 Understanding of the bone remodelling process still remains a challenging topic, as it is a continuous  
74 process that occur throughout one's lifetime. It is now clearly assumed that such a process is initiated  
75 to replace a damaged area of the tissue in order to keep the whole organ healthy [20]. To better  
76 understand this process, the study of the osteonal and interstitial areas appears to be increasingly  
77 interesting, as it will provide a frozen picture of this renewal mechanism at a given time in the process.  
78 Investigating the properties of osteocyte lacunae [43], as well as mineralization on both sides of the  
79 cement line, will improve our knowledge of the relationship between bone 3D architecture and the  
80 role of osteons and cement lines in the orchestration of bone remodelling. In this study, we

81 hypothesize that the cement line is a real structural and biological barrier that separates two different  
82 tissues having specific structural properties and that these properties reflect specific biological activity.  
83 Thus, the aim of this study is to assess the morphometric parameters of the osteonal system on eight  
84 human radii cortical bone samples using SR quantitative phase  $\mu$ CT to investigate the whether there  
85 is an observable and quantifiable difference in terms of osteocyte lacunae morphological organization  
86 between the osteonal and the interstitial tissue.

## 87 **2. Materials and Methods**

### 88 2.1. Bone samples

89 In this study, bones samples were prepared from eight female donors ( $70.3 \pm 13.7$  y.o.; min / max: 50  
90 / 91). The whole radii were extracted from fresh cadavers (French Ministry of Education and Research,  
91 authorization no. DC-2015-2357). The bones were provided by the Departement Universitaire  
92 d'Anatomie Rockefeller (Lyon, France) through the French program on voluntary corpse donation to  
93 science. No information regarding donor' disease or medication history was available, except for the  
94 absence of hepatitis and human immunodeficiency virus. The bones were frozen at  $-20^{\circ}\text{C}$  and covered  
95 with a saline-soaked gauze to maintain hydration until sample preparation.

### 96 2.2. Sample preparation

97 A rectangular sample was harvested from each radius using a low speed saw with a diamond-coated  
98 blade (ISOMET 4000, Buehler, USA). The samples were taken from the anterior region of the bone at  
99 nearly 70 mm from the proximal epiphysis in the middle area between the endosteum and the  
100 periosteum. This area corresponds to that used in a previous study involving the characterization of  
101 bone using guided waves [47]. Before performing SR- $\mu$ CT imaging at the sub-micrometer scale, the  
102 samples were dehydrated to avoid blur artefact in the image. The preparation protocol used was the  
103 same as in a previous study [48], where this protocol was shown to produce artefactual microdamage  
104 of about 25 % in trabecular bone. The samples were placed in acetone, rinsed in water, fixed in 70%  
105 ethanol solution and then dehydrated in a gradually increasing concentration of ethanol (from 70% to  
106 100% spread over 48 hours), thus minimizing damage or cracks. The final dimensions of the samples  
107 used for imaging were  $W = 2.02 \pm 0.09$  mm in the periosteum – endosteum direction,  $B = 1.00 \pm 0.06$   
108 mm in the direction tangential to the bone section, and approximately 12.5 mm in the direction parallel  
109 to the long axis of the diaphysis in order to ensure proper clamping of the sample during images  
110 acquisition.

### 111 2.3. Synchrotron Radiation Micro-Computed Tomography (SR- $\mu$ CT)

112 Image acquisition was performed on beamline ID19 at the European Synchrotron Radiation Facility  
113 (ESRF) in Grenoble, France. A “pink beam” filtered undulator radiation with an effective energy of 31  
114 keV was used. It was obtained from a single-harmonic undulator U17.6 with an undulator gap set to  
115 11.5 mm with a 5.6 mm-thick Al filter and a 1 mm diamond filter. Under these conditions, the FWHM  
116 was estimated to 6keV. The detector was made of a scintillator screen, a visible light microscope, and  
117 a CCD camera. The effective pixel size on the detector was  $0.7 \mu\text{m}$ , and the detector's field of view was  
118  $1.4 \times 1.4 \text{ mm}^2$ . A total of 2000 projection images were recorded over a rotation of  $360^{\circ}$ , with a counting  
119 time of 0.3 s resulting in a scan time of 14 minutes for each sample. The sample-to-detector distance

120 was set to 40 mm to record phase contrast. The images were reconstructed with and without phase  
121 retrieval. Phase retrieval was performed using Paganin's method [49], with the value of  $\delta/\beta$  set at 572.  
122 The volume reconstructions for the eight samples were performed using a filtered-back projection  
123 algorithm yielding 3D images with  $2048^3$  voxels. The size of the bone samples' Volume Of Interest (VOI)  
124 was approximately  $1 \times 1.4 \times 1.4 \text{ mm}^3$ , with the 1 mm dimension corresponding to thickness B of the  
125 sample (cf. 2.2) (Figure1).

## 126 2.4. Image segmentation

127 Image analysis consisted of an investigation of osteonal canals, osteons, lacunae, and micro-cracks  
128 within the VOIs.

### 129 2.4.1. Segmentation of the canals

130 Segmentation of these different structural features was performed automatically on the  $1 \times 1.4 \times 1.4$   
131  $\text{mm}^3$  volumes using the same method, as stated in a previous study [43].

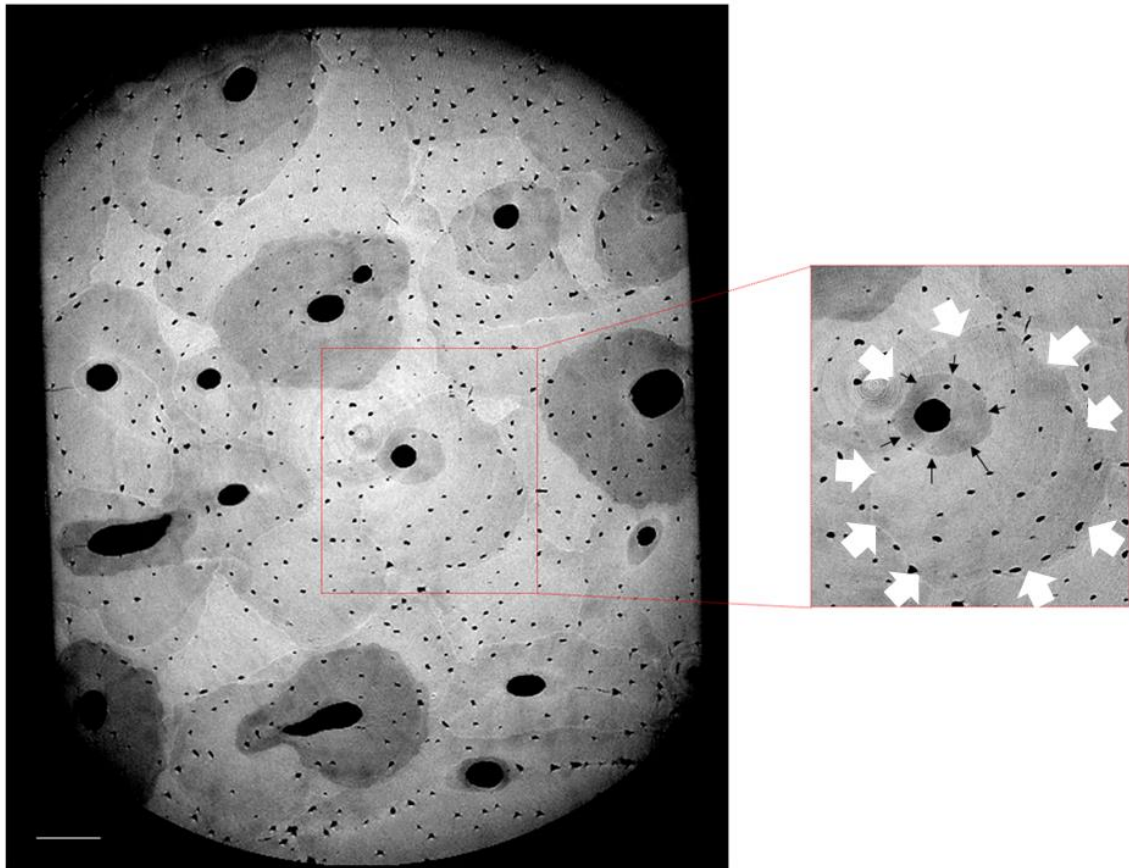
132 We first separated the osteonal canals from other porosities. A bone mask was generated by applying  
133 a median filter to the volume and a threshold using the Otsu method. Lacunae and micro-cracks ( $< 30$   
134  $\mu\text{m}$ ) were removed by applying a threshold on the size of each object after performing a connected  
135 component analysis. The canal mask was then considered as the complement of the bone mask.

### 136 2.4.2. Segmentation of the osteons

137 Osteon segmentation was performed manually using Avizo software (Thermal Fischer Scientific) on the  
138 phase-retrieved volume. For each osteon, the interface between osteonal and interstitial tissue was  
139 delineated in slices perpendicular to the main axis of the bone diaphysis. The segmented objects were  
140 defined by all of the pixels within the delineated interface. An interpolation tool provided by the  
141 software was used to avoid performing contouring on each slice. The interpolation step depended on  
142 the shape evolution of each osteon, from  $5 \mu\text{m}$  when the osteon's shape changed considerably in  
143 relation to the slice (for example, when two osteons joined together) to  $50 \mu\text{m}$  when the shape of the  
144 osteons was almost constant along the diaphysis (almost cylindrical). A complete segmentation of the  
145 VOI provides a binary volume with all of the segmented objects. Then the canals mask was subtracted  
146 from this binary volume in order to only have the osteons mask and its complementary volume, which  
147 would be the interstitial tissue mask (Figure 1). A similar procedure has been applied by Maggiano et  
148 al., [50].

149 Osteons can be distinguished from interstitial tissue due to their differences in grey levels, which  
150 correspond to their differences in mineralization, which is enhanced in a X-Ray phase CT (Figure 1). For  
151 some cases, two different osteons could be seen around a single canal, showing that bone remodelling  
152 is a dynamic process. In such a case, the osteon that was closer to the canal (meaning the younger  
153 osteon (Figure 1b)) was chosen.

154



a.

b.



c.

d.

e.

f.

g.

155 **Figure 1 a.: VOI phase contrast slice from a radius sample of a female donor (50 y.o.), b.:**  
 156 **Cropped image of a single osteon. Note the two interfaces (white and black arrows). The**  
 157 **chosen interface is the one closer to the canal pointed by the black arrows. Following figures:**  
 158 **binary-segmented volumes of c.: Haversian or Volkmann canals mask, d.: total osteon mask,**  
 159 **e.: osteons mask (canals subtracted), f.: interstitial mask, g.: Lacunae and micro-cracks mask.**  
 160 **Scale bars = 100  $\mu$ m. Note the distinct osteons around the canals in darker gray than the**  
 161 **surrounding interstitial tissue.**

#### 162 2.4.3. Segmentation of lacunae and micro-cracks

163 Lacunae and micro-cracks were then segmented automatically using the following process. First,  
 164 hysteresis thresholding was applied to the volume within the bone mask, resulting in a binary volume  
 165 containing both lacunae and micro-cracks (Figure 1g) [43]. From this volume, a connected component  
 166 analysis was performed to label each object (either lacuna (Lc) or micro-crack ( $\mu$ Cr)), and geometric

167 descriptors of these objects were calculated [3]. In this study, each object is considered as an ellipsoid  
 168 with three main axes (L1, L2, and L3 in  $\mu\text{m}$ ). Lacunae and micro-cracks were then separated into two  
 169 classes of objects distinguished by morphometric criteria such as volume (V in  $\mu\text{m}^3$ ), thickness (Th in  
 170  $\mu\text{m}$ ), aspect ratios or Structural Model Index (SMI), or Euler number ( $\chi$ ) [51]. The calculations for these  
 171 parameters are given in [3,43]. The micro-crack criteria used in the current study were inspired by the  
 172 criteria used in [43], with some slight differences. Table 1 gives a summary of the criteria used for the  
 173 segments for only osteocytes lacunae or micro-cracks.

174 **Table 1 Inclusion morphometric criteria for the segmentation of the osteocyte lacunae (Lc) or**  
 175 **of the micro-cracks ( $\mu\text{Cr}$ ) [43]**

| Osteocytes lacunae   | Micro-cracks  |
|--|---|
| Lc.V > 82 $\mu\text{m}^3$ and Lc.V < 10000 $\mu\text{m}^3$ | $\mu\text{Cr.V} > 500 \mu\text{m}^3$  |
| Lc.L1/Lc.L3 < 15 and Lc.L2/Lc.L3 < 8                       | $\mu\text{Cr.L1}\mu\text{Cr.Th} > 15$ , $\mu\text{Cr.L2}/\mu\text{Cr.Th} > 11$ and<br>$\mu\text{Cr.L3}/\mu\text{Cr.Th} > 1.5$ |
| Lc.SMI > 1.6   | $\mu\text{Cr.Th} < 4$   |
| $0 < \text{Lc.}\chi < 2$                                   | $\mu\text{Cr.SMI} < 2.5$  |

176 After the automatic segmentation, manual refinement was performed within the micro-cracks volume  
 177 to eliminate any artefacts, such as large lacunae that look like micro-cracks.

## 178 2.5. Image Analysis

179 The nomenclature for the analysed parameters in the current study were defined according to bone  
 180 histomorphometry standardization [52,53].

### 181 2.5.1. Canals analysis.

183 Osteonal canals –(On.Ca) were analysed using CTAn (CT Analyser Software V 1.14.4, Skyscan NV,  
 184 Kontich, Belgium). On these VOIs, the canal volume fraction On.Ca.V/TV (%) was quantified. Total  
 185 Volume (TV, in  $\text{mm}^3$ ) was measured by adding the voxels of the canal mask On.Ca.V ( $\text{mm}^3$ ) and those  
 186 of the bone mask BV ( $\text{mm}^3$ ). Mean canal diameter On.Ca.Dm ( $\mu\text{m}$ ) was also measured as the value of  
 187 the maximal fitting sphere within the structure [54].

### 188 2.5.2. Osteon analysis

189 Osteons were also analysed using CTAn (CTAnalyser Software V 1.14.4, Skyscan NV, Kontich, Belgium).  
 190 Osteonal volume On.V ( $\text{mm}^3$ ) was measured as the sum of the voxels of the osteonal mask. Osteonal  
 191 volume fraction was measured both as a function of total volume On.V/TV (%) and as a function of  
 192 bone volume On.V/BV (%) because they are present in bone tissue. Diameter On.Dm ( $\mu\text{m}$ ) was also  
 193 measured using the same method as that for the canals and thus was included the canal. Finally, the  
 194 total perimeter of the osteonal system, On.Pm (mm), was calculated as the average value of the

195 perimeter measured slice by slice. This value is an estimation of the total length of the cement line on  
196 each slice. For the latter, the volume including both osteons and canals was used (Figure 1d).

197 The volume of the interstitial tissue  $It.V$  ( $mm^3$ ) was also calculated.

### 198 2.5.3.Lacunae and micro-cracks analysis

199 Regarding lacunae, the dimensions of the three main axes of the best-fitting ellipsoid were analysed  
200 for Lc.L1, Lc.L2, and Lc.L3 ( $\mu m$ ) [3,43]. The ratios Lc.L1/Lc.L2 and Lc.L1/Lc.L3 were also computed. Their  
201 volume fraction Lc.V/BV (%) and density Lc.N/BV ( $mm^{-3}$ ) were quantified. These parameters were  
202 measured with respect to Bone Volume (BV).

203 To analyse the differences between the osteonal and interstitial tissue, the lacunae included in the  
204 osteonal volume and in the interstitial volume were separated, and their properties were calculated  
205 separately. For volume fraction and density, lacunar volume and number were divided by either  
206 osteonal volume (for lacunae within osteons) or interstitial volume (for the other lacunae) (Lc.V/On.V  
207 (%), Lc.N/On.V ( $mm^{-3}$ ) or Lc.V/It.V (%), Lc.N/It.V ( $mm^{-3}$ ), respectively).

208 Micro-cracks volume fraction  $\mu Cr.V/BV$  (%) was also measured.

209 As for the lacunae, micro-cracks within the osteons or within the interstitial tissue were then analysed  
210 separately and provided the following quantities:  $\mu Cr.V/On.V$  (%) or  $\mu Cr.V/It.V$  (%).

### 211 2.5.4. Bone mass density

212 Bone mass density,  $\rho$  ( $g.cm^{-3}$ ) was calculated from the reconstructed image using the following  
213 equation [25]:

$$\rho (g.cm^{-3}) = \frac{\delta}{\beta} \cdot \frac{\mu \cdot 10^{-1}}{4\pi \cdot 1.3 \cdot \lambda} \quad \text{with} \quad \frac{\delta}{\beta} = 572 \text{ (cf. 2.3)}, \quad (\text{Eq.1})$$

214 where  $\mu$  ( $mm^{-1}$ ) is the linear attenuation coefficient obtained directly as the output of the  
215 reconstructed software, and  $\lambda$  ( $\text{\AA}$ ) is the wavelength of the X-Ray beam ( $\lambda = 0.400 \text{ \AA}$  at 31 keV).

216 Bone mass density was calculated for the complete volume of bone (BV), osteonal volume (On.V),  
217 and interstitial volume (It.V) excluding all porosities (canals, lacunae or micro-cracks).

### 218 2.5.5.Distribution of the lacunar properties with respect to the cement lines (CL)

219 In order to analyse the distribution of the lacunae's properties on both sides of the CL, a CL mask was  
220 first created by calculating the morphological derivate of the osteons mask (*i.e.*, subtracting the dilated  
221 and eroded images). We then calculated the Euclidian distance map of the CL and the Euclidian  
222 distance map from the osteonal canals' boundaries, which provide a volume of the shortest distance  
223 to the CL and a volume of the shortest distance to the canals. For each lacuna in an osteon, the ratio  
224 between its distance to the canal boundaries (value for the canal distance map) and the distance  
225 between the canal and the CL (value for the canals mask's distance map + value for the CL's distance  
226 map) was assigned at its barycentre. A value of 1 corresponds to a lacuna that is at the cement line,  
227 whereas a value of 0 is at the canal boundary. For each lacuna within the interstitial tissue, the ratio  
228 between its distance to the canal (value for the canals mask's distance map) and the distance between

229 the canal and the CL (value for the canals mask's distance map – value for the CL's distance map) was  
230 assigned at its barycentre. A value of 1 corresponds to a lacuna that is on the CL, a value of 2  
231 corresponds to a point at which the distance to the canal is twice that of the distance from canal  
232 boundary to CL. In the following, the value assigned to each lacuna is called the normalised distance.

233 The distance maps were then partitioned into bins of 0.02. For example, the first bin is composed of  
234 voxels with a value of a distance ratio ranging from 0 to 0.02. Lacunae parameters were averaged on  
235 each of these bounded volumes. Lacunar density was also measured by dividing the number of lacunae  
236 within the bin (N.Lc) by the number of voxels within the bin (Bin.V (mm<sup>3</sup>)). Voxels included in the canals  
237 mask were not considered in these bins, because there was no lacuna found in these canals.

238 For the bone mass density, the relative difference ( $\Delta\rho$  in %) between the values of  $\rho$  within the bin and  
239 the mean value obtained for the bone volume was investigated.

240 Values from 0 to 1 correspond to osteons and values from 1 to 2 correspond to interstitial tissue (see  
241 Figure 3).

## 242 2.6. Statistical tests

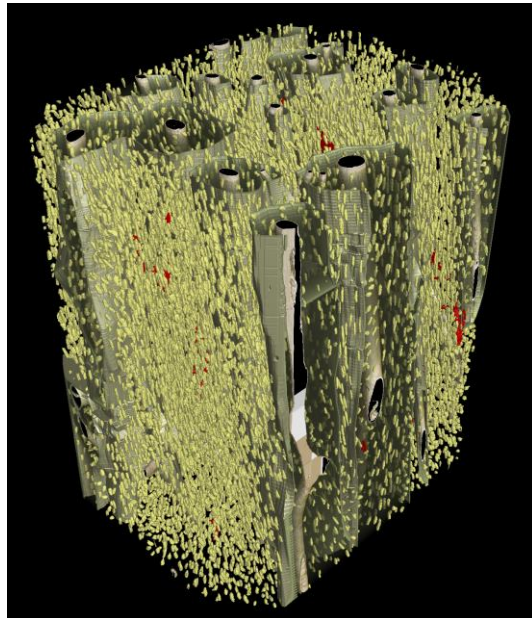
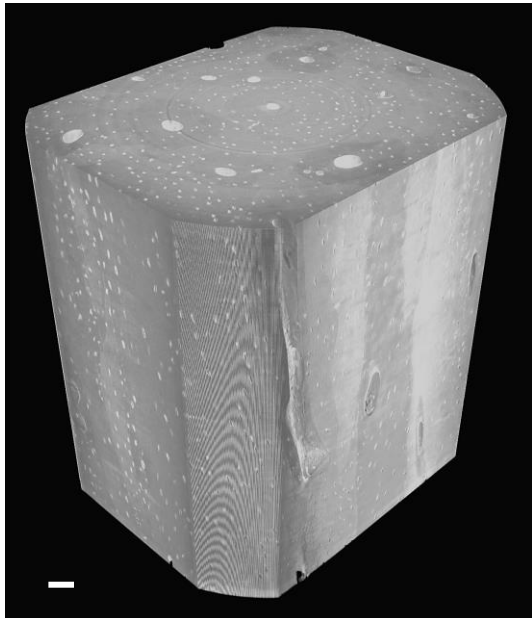
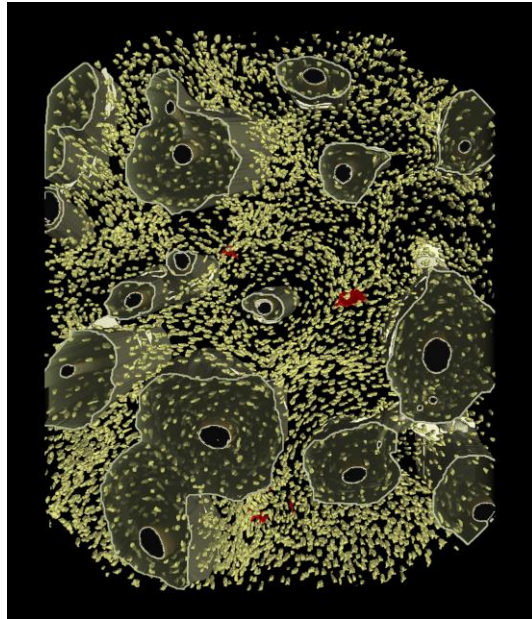
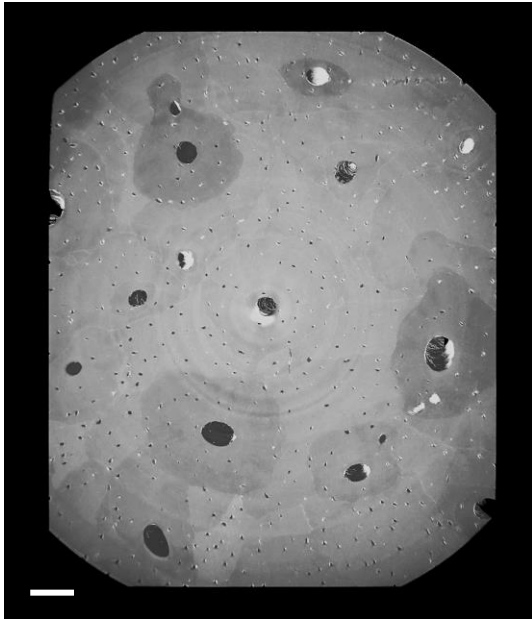
243 A non-parametric Friedman test for independent samples was applied before applying a Wilcoxon test  
244 for paired samples using StatView (SAS Institute Inc., USA) to analyse differences between osteonal  
245 and interstitial tissue. Correlations were analysed by measuring the Spearman coefficient. Results with  
246 p-value < 0.05 were considered as significant.

247 The Spearman's coefficient between the osteonal morphometric parameters and osteonal canals,  
248 lacunae, and micro-cracks parameters was measured.

## 249 3. Results

250 Figure 2 shows the 3D rendering of the VOI obtained from the radius of a female donor after  
251 segmentation (50 y.o.).

252



a.

b.

253 **Figure 2** 3D rendering of the VOI from a donor (50 y.o.) under two orientations. a. phase  
254 contrast; b.: segmented volume. Note in olive-green the osteons, in yellow the osteocytes  
255 lacunae and in red the micro-cracks. Scale bar = 100  $\mu\text{m}$ .

256 3.1. Canals analysis

257 Morphometric values measured for Haversian canals are given in Table 2.

258 **Table 2 Morphometric parameters of Haversian canals**

| Morphometric parameters    | Average (SD) |
|----------------------------|--------------|
| On.Ca.V/TV (%)             | 4.5 (2.1)    |
| On.Ca.Dm ( $\mu\text{m}$ ) | 64.7 (23.1)  |

259 3.2. Osteon analysis

260 Morphometric values obtained for osteonal system are given in Table 3.

261 **Table 3 Morphometric parameters of osteons**

| Morphometric parameters | Average (SD) |
|-------------------------|--------------|
| On.V/TV (%)             | 40.9 (6.8)   |
| On.V/BV (%)             | 43.2 (8.4)   |
| On.Dm ( $\mu\text{m}$ ) | 184.0 (13.3) |
| On.Pm (mm)              | 5.6 (0.8)    |

262 3.3. Lacunar and micro-cracks analysis

263 Table 4 and Table 5 show lacunar and micro-cracks morphometric parameters, respectively, for the  
264 total volume, in osteons and in interstitial tissue.

265 There were significant differences between the lacunar properties in osteons and those in the  
266 interstitial tissue. Lacunar density is 11.8 % higher in the osteonal tissue compared to the interstitial  
267 tissue. Lc.L1 is 6.4 % higher in the interstitial tissue resulting in a Lc.L1/Lc.L2 10 % higher in the  
268 interstitial tissue and a Lc. $\rho_1$  15.8 % higher in osteonal tissue.

269 85 % of the micro-cracks were observed within interstitial tissue.

270 **Table 4 Lacunar morphometric parameters. Note that for the osteon and interstitial tissue, BV =**  
 271 **Ost.V or Inter.V, respectively (Average (SD)).**

| <b>Morphometric parameters</b> | <b>Bone</b>          | <b>Osteon</b>       | <b>Interstitial tissue</b> |
|--------------------------------|----------------------|---------------------|----------------------------|
| Lc.V/BV (%)                    | 1.2 (0.1)            | 1.1 (0.4)           | 1.3 (0.1)                  |
| Lc.N                           | 32609                | 15035               | 17574                      |
| Lc.N/BV (mm <sup>-3</sup> )    | <b>19621 (2171)*</b> | <b>20832 (2522)</b> | <b>18621 (1682)</b>        |
| Lc.L1 (µm)                     | <b>25.3 (2.5)*</b>   | <b>24.5 (2.0)</b>   | <b>26.2 (3.3)</b>          |
| Lc.L2 (µm)                     | 10.9 (0.7)           | 11.22 (1.0)         | 10.8 (0.6)                 |
| Lc.L3 (µm)                     | 5.3 (0.2)            | 5.3 (0.2)           | 5.3 (0.3)                  |
| Lc.L1/Lc.L2                    | <b>2.3 (0.3)*</b>    | <b>2.2 (0.2)</b>    | <b>2.4 (0.3)</b>           |
| Lc.L1/Lc.L3                    | 4.8 (0.5)            | 4.7 (0.4)           | 5.0 (0.8)                  |

*\*significant difference between osteonal and interstitial tissue (p-value < 0.05)*

272 **Table 5 Micro-cracks morphometric parameters. Note that for the osteon and interstitial tissue,**  
 273 **BV = Ost.V or Inter.V, respectively (Average (SD)).**

| <b>Morphometric parameters</b>  | <b>Bone</b>       | <b>Osteon</b>    | <b>Interstitial tissue</b> |
|---------------------------------|-------------------|------------------|----------------------------|
| µCr.V/BV (% x 10 <sup>3</sup> ) | <b>8.3 (7.4)*</b> | <b>2.4 (2.9)</b> | <b>12.2 (10.2)</b>         |

*\*significant difference between osteonal and interstitial tissue (p-value < 0.05)*

274 3.4. Bone mass density

275 Table 6 shows bone mass density values obtained for bone volume, osteonal and interstitial volumes.  
 276 There was a significant difference measured between osteonal and interstitial volumes, with an  
 277 osteonal value of mass density 5.6 % lower.

278 **Table 6 Bone mass density. Note that for the osteon and interstitial tissue, BV = Ost.V or**  
 279 **Inter.V, respectively (Average (SD)).**

| <b>Morphometric parameters</b> | <b>Bone</b>         | <b>Osteon</b>      | <b>Interstitial tissue</b> |
|--------------------------------|---------------------|--------------------|----------------------------|
| ρ (g.cm <sup>-3</sup> )        | <b>1.68 (0.04)*</b> | <b>1.62 (0.06)</b> | <b>1.72 (0.03)</b>         |

*\*significant difference between osteonal and interstitial tissue (p-value < 0.05)*

280 3.5. Correlations

281 Table 7 gives the Spearman's coefficient between morphometric parameters of osteons and the other  
 282 structural features.

283 A significant correlation was observed between the canal and osteon volume fraction.

284 Regarding the osteocyte lacunae, there were significant correlations between the osteonal volume  
 285 fraction On.V/BV and Lc.L1, Lc.L1/Lc.L2 and Lc.p<sub>1</sub>. The osteonal perimeter Ost.pm also has a strong  
 286 correlation with Lc.N/BV, Lc.L1, Lc.L1/Lc.L2 and Lc.L1/Lc.L3. There was no significant correlation for  
 287 osteonal diameter On.Dm.

288 Finally, the micro-cracks volume fraction is significantly correlated with the osteonal volume fraction,  
 289 but there was no correlation between crack volume fraction and osteonal diameter or perimeter.

290 There was no correlation between any of the morphometric parameters and the age of donors.

291 Table 7 Spearman's coefficient between osteonal and Haversian canals, lacunar and micro-cracks  
 292 morphometric parameters

| Haversian canals   |               |         |         |          |        |             |             |
|--------------------|---------------|---------|---------|----------|--------|-------------|-------------|
|                    | On.Ca.V/TV    |         |         | On.Ca.Dm |        |             |             |
| On.V/BV            | 0.88*         |         |         | 0.67     |        |             |             |
| On.Dm              | 0.47          |         |         | 0.48     |        |             |             |
| On.Pm              | 0.56          |         |         | 0.33     |        |             |             |
| Osteocytes lacunae |               |         |         |          |        |             |             |
|                    | Lc.V/BV       | Lc.N/BV | Lc.L1   | Lc.L2    | Lc.L3  | Lc.L1/Lc.L2 | Lc.L1/Lc.L3 |
| On.V/BV            | 0.17          | 0.60    | - 0.71* | 0.31     | - 0.24 | - 0.91*     | - 0.57      |
| On.Dm              | - 0.41        | - 0.24  | 0.05    | - 0.17   | - 0.40 | 0.04        | 0.08        |
| On.Pm              | 0.31          | 0.83*   | - 0.95* | 0.07     | 0.19   | - 0.81*     | - 0.91*     |
| Micro-cracks       |               |         |         |          |        |             |             |
|                    | $\mu$ Cr.V/BV |         |         |          |        |             |             |
| On.V/BV            | - 0.74*       |         |         |          |        |             |             |
| On.Dm              | 0.18          |         |         |          |        |             |             |
| On.Pm              | - 0.69        |         |         |          |        |             |             |

\* p-value < 0.05

293 3.6. Distribution of the lacunar properties with respect to the CL

294 Figure 3 gives an example of the distributions of lacunae properties within the osteon expressed as a  
 295 function of the normalized distance to the canal. Figure S1 in the supplementary materials shows the  
 296 gathered data for all the donors. These curves are reported from one female donor (50 y.o.), but they  
 297 are representative of all of the distributions obtained for the eight donors. For all of the parameters,  
 298 variation is seen within the osteon and almost no variation is observed in the interstitial tissue.

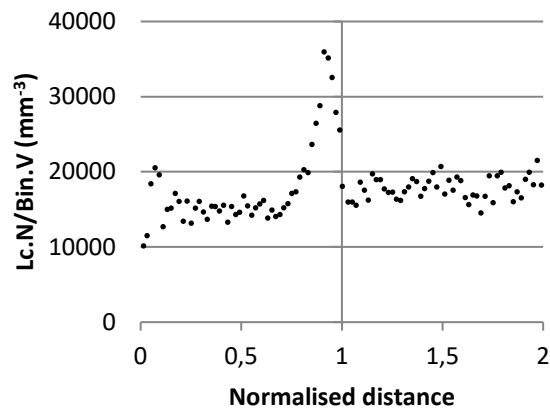
299 Lacunar density (Figure 3a) increases by almost 100 %, from 15000 to 30000 mm<sup>-3</sup>, near the cement  
 300 line before decreasing at the cement line. The bell part of the curve ranges from 0.75 to 1.

301 The variation for Lc.L1 (Figure 3b) in the osteon is a bell curve that ranges between the canal and the  
 302 CL, with a maximum value at the middle of the osteon and drops close to the CL. The values at the  
 303 canal and at the CL are nearly the same.

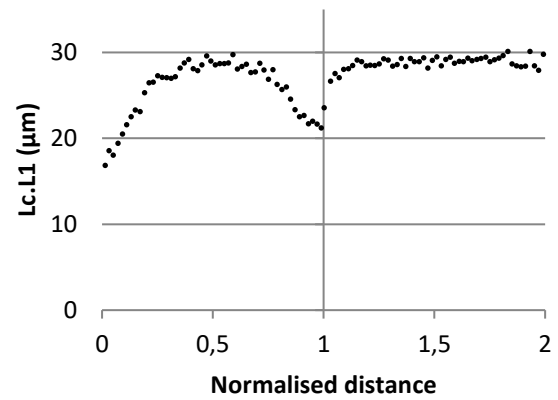
304 Lc.L2 (Figure 3c) and Lc.L3 (Figure 3d) show the same kind of variation, with a maximum value near the  
 305 CL and a slight decrease before the canal. For Lc.L3, the decrease increases near the canal, from a  
 306 distance ratio of 0.15 to 0.

307 The aspect ratio Lc.L1/Lc.L2 (Figure 3e) has the same kind of variation as Lc.L1, thus highlighting the  
 308 higher variation of Lc.L1 than Lc.L2.

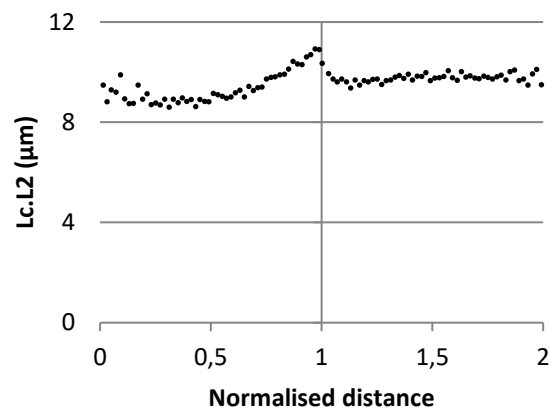
309 Regarding  $\Delta\rho$  (Figure 3f), the interesting point is an increase at the CL.



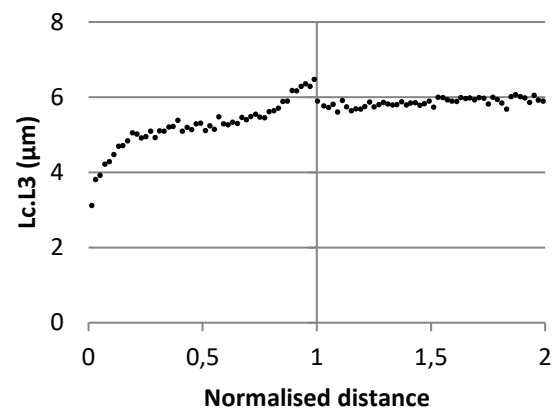
a.



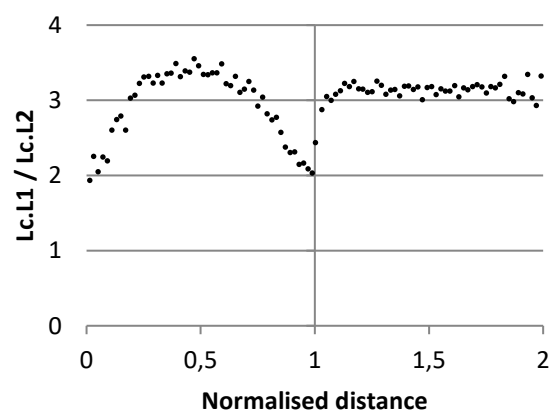
b.



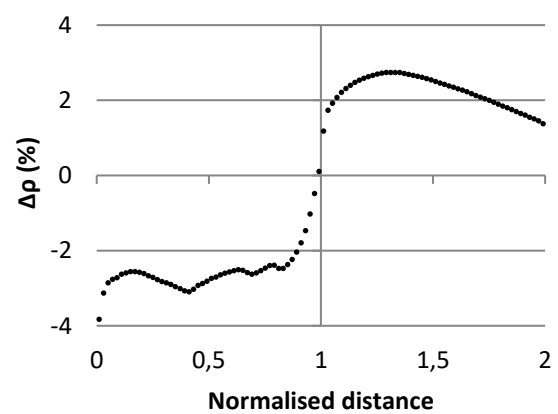
c.



d.



e.



f.

310 **Figure 3** Distributions of the lacunar morphometric parameters from the CL for a radius sample  
311 of a female donor (50 y.o.). Values between 0 and 1 correspond to the osteon; the CL is at the

312 **ratio distance 1. a.: lacunar density in each bin, b.: Lc.L1, c.: Lc.L2, d.: Lc.L3, e. Lc.L1/Lc.L2 and**  
313 **f.: $\Delta\rho$ .**

314

#### 315 **4. Discussion**

316 This study investigated the 3D properties of the osteonal system in human cortical bone samples  
317 extracted from the radius of eight female donors using SR- $\mu$ CT. To the best of our knowledge, this is  
318 the first time that such a data set on bone microstructure has been obtained.

319 Previous data on cortical bone osteons were mainly obtained using 2D techniques, which makes it  
320 difficult to compare to our results. In 2000, Yeni et al. performed histological analyses on samples  
321 harvested from femoral necks [41]. The values of canal and osteonal volume fractions found in the  
322 current study are of the same order of magnitude as the values of canal and osteonal area fractions  
323 found by Yeni et al. ( $4.1 \pm 2.1\%$  /  $43.2 \pm 8.4\%$  in the current study,  $6.75 \pm 2.62\%$  /  $48.17 \pm 14.57\%$ , in  
324 [41], respectively, for the canal / osteonal fractions). In the previous study, analyses were performed  
325 on human femoral neck samples compared to the human radii in the current study, which can partly  
326 explain the slight differences. In the same way, the diameters of the Haversian canals and the osteons  
327 obtained in the current study in 3D (On.Ca.Dm =  $64.7 \pm 23.1\ \mu\text{m}$  / On.Dm =  $184.0 \pm 13.3\ \mu\text{m}$ ) are of the  
328 same order of magnitude as the previous results found in 2D using histology (On.Dm =  $193.35 \pm 10.98$   
329  $\mu\text{m}$  in [14]) or scanning electronic microscopy (On.Ca.Dm =  $69.71 \pm 35.95\ \mu\text{m}$  / On.Dm =  $156.31 \pm 51.09$   
330  $\mu\text{m}$  in [24]). These two previous studies investigated human femoral diaphyses [14,24]. Since the  
331 authors previously found evidence of significant differences in the canal's architecture in the radius  
332 compared to the femoral diaphysis [43], the differences in osteons can be expected at these two  
333 anatomical locations.

334 It is interesting to observe that the volume fraction of osteons is correlated with the volume fraction  
335 of the osteonal canals. This correlation highlights that tissue with a high amount of Haversian porosity  
336 will present a higher amount of osteons than tissue with a lower Haversian porosity. This result is  
337 consistent, since the osteons arise through a bone remodelling process that is initiated at the osteonal  
338 canals. When the signal is sent to remodel a damaged area, osteoclasts initiate the resorption step  
339 along osteonal canals. Once this resorption step is concluded, the cement line is deposited, and bone  
340 deposition by osteoblasts initiates along the bone surface available in the osteonal canals [16,18,55].  
341 Bone tissue with a higher amount of Haversian canals will present more sites for the initiation of the  
342 remodelling process. Still no correlation was found between the osteonal and Haversian canals  
343 diameters (On.Dm and On.Ca.Dm). This is consistent with the way in which the bone remodelling  
344 process is undergone. In the early stage of the remodelling process, osteoclasts first initiate resorption,  
345 which yield to the creation of a cutting cone, and then this cutting cone is widened in order to resorb  
346 all of the damaged tissue. The formation of bone is then initiated on the wall of the cutting cone. This  
347 process shows that the size of the cutting cone will vary all along its length [16,56].

348 The averaged values for the osteocytes lacunae obtained have already been discussed in [43]. The  
349 values are slightly different because, in the current study, a larger volume of interest was analysed  
350 (e.g., Lc.L1 =  $25.3\ (2.5)\ \mu\text{m}$  in the current study and Lc.L1 =  $25.7\ (2.2)$  in [43]). We found significant  
351 differences in the lacunae density, lacunae main length, and anisotropy between the osteonal and  
352 interstitial tissues. To the best of our knowledge, there is no equivalent data in the literature. Some

353 studies have nevertheless been performed to assess the lacunae morphometric parameters within the  
354 osteonal tissue alone, without investigating the differences with the interstitial tissue [29–31,57,58].  
355 We can state that the significant differences between properties of the osteonal and interstitial tissues  
356 arise mainly due to variations observed within osteons. For example, lacunar density is nearly constant  
357 in osteonal tissue close to the canal or in interstitial tissue, but a high peak is observed close to the CL.  
358 This peak increases the averaged value measured in the osteonal tissue. Similar results regarding  
359 variation in lacunar density have already been observed in the past, both in 2D [31] and in 3D [30]. In  
360 these studies, a variation of lacunar density was measured as a function of the distance to the cement  
361 line of the osteon. In particular, a decrease in this density was measured as we move away from the  
362 cement line. However, these studies were performed on only one subject, either in 2D [31] or in 3D,  
363 assuming a constant contour along 835  $\mu\text{m}$  [30]. The current study involves 3D VOIs obtained from  
364 eight donors involving an average of 32609 lacunae on each VOI. Moreover, the segmentation of  
365 osteons is more realistic than in that of [30]. It is known that osteocytes are former osteoblasts that  
366 are embedded within the bone matrix after deposition of tissue [59,60]. The bone deposition rate by  
367 the osteoblast during the bone remodelling process decreases from the beginning until the end of the  
368 deposition process, and the osteocytes density was related to the deposition rate [61–64]. As the CL is  
369 the interface at which bone deposition begins [65], the higher osteocyte lacunae density near this CL  
370 may reflect the higher activity of these osteoblasts at the beginning of the bone remodelling process.  
371 In a previous study, Repp et al. investigated the spatial heterogeneity of the canaliculi within the  
372 osteons [66]; the canaliculi are small canals less than 0.40  $\mu\text{m}$  in diameter that connect the osteocytes  
373 between them and form the lacuna-canalicular network [67]. Their results showed that the density of  
374 canaliculi vary from the canal surface to the cement lines in the opposite way compared to the lacunae  
375 density in the current study, the density of canaliculi is higher near the Haversian canal surface [66]. It  
376 would be interesting to investigate the relationships between the canaliculi density and osteocytes  
377 morphometric parameters measured in the current study. However, the parameters used for the  
378 imaging protocol in the current study do not allow the investigation of such features.

379 In a previous study, Atkinson et al. also observed that the lacunae near the CL were larger than the  
380 lacunae near the canal [57]. As their study was performed in 2D and perpendicular to the osteon, the  
381 long axis of lacunae that they consider corresponds to Lc.L2 measured in the current study [3]. Our  
382 results show a slight increase of Lc.L2 from the canals boundary to the CL (Figure 3). In a previous study,  
383 Ardizzoni observed a relation between a decrease in the thickness of the lamellae that made bone  
384 tissue from the CL to the canal and lacunae size [29]. He assumed that lamellae are thinner near the  
385 canal because of the decrease in the size of osteocytes and, more specifically, the decrease in the size  
386 of the former osteoblasts before their differentiation in osteocytes. Our results regarding Lc.L1 and for  
387 Lc.L1/Lc.L2 and Lc. $\rho_1$  are original, as most previous studies were performed in 2D on a section  
388 perpendicular to the osteon, whereas osteocyte lacunae are oriented parallel to the osteon [3].  
389 Considering the previous hypothesis that osteocytes dimensions have an influence on bone deposition,  
390 these results strongly suggest that bone formation goes through different steps between the start of  
391 the deposition at the cement line until the end of the process, as reflected by the bell curves in Figure  
392 3. The importance of the CL in terms of lacunar system organization is also highlighted due to the  
393 correlations found between osteonal and lacunar parameters, more specifically with the osteons  
394 perimeter (see Table 7).

395 The lack of variation in the lacunar geometry observed within the interstitial tissue uncovers several  
396 questions. One explanation could be that, since the interstitial tissue is in reality a mixture of fragments

397 of older osteons, the possible variations of lacunar geometry properties could be averaged when  
398 considering only the distance to the cement line. Another explanation for the differences in the lacunar  
399 geometry between the osteonal and interstitial tissue, but also regarding the variation within one  
400 osteon, could be found in the perilacunar remodelling that might occur in the local environment of the  
401 osteocytes, meaning that remodelling (resorption/deposition of bone tissue) might still occur after the  
402 differentiation of osteoblasts into osteocytes. This topic has long been a topic of discussion, but recent  
403 studies demonstrate that such a process occurs in bone tissue [67–72]. Under this hypothesis, the  
404 geometry of the osteocyte lacunae, once embedded in the bone matrix, can evolve over time [73]. This  
405 perilacunar remodelling can occur either in the osteon or in the interstitial tissue.

406 The micro-crack volume fraction obtained in the current study is larger than the value found in a  
407 previous study on smaller VOIs ( $8.3 \times 10^{-3} \pm 7.4 \times 10^{-3} \%$  in the current study,  $24.32 \times 10^{-3} \pm 17.66 \times 10^{-3}$   
408  $\%$  in [43]). The differences might be explained by the slight difference in the choice of the  
409 morphometric criteria and manual refinement of the segmentation that was performed in the current  
410 study. This refinement was not performed in [43] because of the large number of analysed volumes.  
411 Moreover, in the current study, the size of the VOIs is much larger than in the previous study. Still, the  
412 value of  $\mu\text{Cr.V/BV}$  is very small. In the current study, we observed a large difference of 75 % between  
413 the osteonal and interstitial tissue. This is in accordance with previous results showing that micro-  
414 cracks are mainly initiated in the interstitial tissue that is more mineralized, whereas cement lines act  
415 as barriers to these cracks [8,74,75]. Schaffler et al. also found that 85 % of the micro-cracks included  
416 in bone are observed in the interstitial tissue. This observation might be explained by the difference in  
417 mineralisation between the interstitial and the osteonal tissue. A more mineralised tissue (i.e. a stiffer  
418 tissue [76]) is indeed a preferential area for the initiation and the propagation of cracks [77].

419 The mass density values obtained in the current study are comparable to the bone mass density data  
420 obtained in a previous study from our group investigation of cortical bone sample using SR- $\mu\text{CT}$  [25].  
421 The difference in the bone mass density found between osteonal and interstitial tissue was expected,  
422 since osteon is a younger tissue that arises from the remodelling process [21–23,28]. However, this  
423 difference is small (5.6 %), which explains the difficulty in automatically segmenting osteons from  
424 interstitial tissue. A study by Langer et al. revealed a higher density at the CL that was not observed in  
425 the current study [25]. In this previous study, the resolution was higher than in the current study (pixel  
426 size of 60 nm in [25] and  $0.7 \mu\text{m}$  in the current study). This higher resolution allows for better  
427 visualisation of these cement lines, as they are interfaces that are less than  $5 \mu\text{m}$  in thickness [55].

428 It should be noted that the current study has been performed on the radius of eight female donors  
429 aged from 50 to 91 y.o. It is widely known that anatomical location [43,78], gender [79,80], and age  
430 [14,81] influence bone microstructure. This means that the results obtained correspond to a specific  
431 population and cannot be generalized to a larger population of younger or male donors.

432 It is also worth noting that, in such cortical bone samples, what is called interstitial tissue is composed  
433 of different fragments of old osteonal tissue that, with time, have reached a higher level of  
434 mineralization and are less distinguishable, as seen in Figure 1. The results of the current study were  
435 obtained by selecting only the smaller osteon adjacent to each canal, referring to the smaller osteon  
436 in the case that there are two concentric osteons. This means that our osteon data set represents a  
437 population of new osteons (see Figure 1b).

438 The author acknowledge that the cutting and preparation protocols are likely to introduce micro-  
439 cracks. The influence of ethanol drying procedure as used in the current study was shown to induce  
440 artefactual micro-cracks of about 25 % (of 100 % detected) when analysed using optical microscopy  
441 [48]. As this past study was done on trabecular and not cortical human bone, the proportion of pre-  
442 existing and induced micro-cracks cannot be elucidated in the present study but may be in a similar  
443 range.

444 The size of the VOIs used in the current study can also be considered as small ( $1 \times 1.4 \times 1.4 \text{ mm}^3$ ). A  
445 previous study revealed that there was no difference between osteonal canals morphometric  
446 parameters measured on two contiguous VOIs of  $1 \times 1.4 \times 1.4 \text{ mm}^3$ , as in the current study. Even if the  
447 osteonal canals are smaller than osteons, they are correlated (see Table 7). This conforms to the results  
448 obtained in the current study on the osteonal system.

449 The number of donors used in this study is small (eight donors). In a previous study, we performed a  
450 total of 48 scans on paired femoral diaphyses, femoral necks, and radial diaphyses both on control and  
451 fractured VOIs [12,43]. But as the manual segmentation of the osteons is highly time consuming, the  
452 authors chose first to perform the investigation on a sub-population of these 48 scans. Regarding the  
453 results obtained, it is obvious that enlarging the study to include femoral diaphyses and necks would  
454 be of great interest to assess the influence of anatomical location. Furthermore, the investigation of  
455 the influence of the osteonal system on bone crack propagation mechanisms would also be of great  
456 interest to better understand the bone fracture process.

## 457 **5. Conclusions**

458 The current study investigated the osteonal systems of eight female donor radii in three dimensions.  
459 Novel results were obtained regarding the morphometric parameters of the osteons. The  
460 morphometric parameters of osteocyte lacunae appear to follow a specific distribution between the  
461 Haversian canal surface and the cement line. The importance of cement lines in bone architecture has  
462 been highlighted. The structural differences on both sides of the cement lines strongly suggest a  
463 different biological activity between osteonal and interstitial tissue.

## 464 **Conflict of interests**

465 The authors declare no conflict of interest. The funding sponsors had no role in the design of the study;  
466 in the collection, analyses, or interpretation of data; in the writing of the manuscript, and in the  
467 decision to publish the results.

## 468 **Acknowledgments**

469 The authors acknowledge the ESRF ID19 staff for his support for synchrotron data acquisition during  
470 the experiment MD923. This work was partly funded by the LabEx PRIMES, France (ANR-11-LABX-0063)  
471 within the program "Investissements d'Avenir", France (ANR-11-IDEX-0007). This study was also partly  
472 funded by the Région Auvergne- Rhône-Alpes, France (14-011125-01). This work was also done in the  
473 context of the ANR project MULTIPS (ANR-13-BS09-0006) and of the project France Life Imaging (ANR-  
474 11-INBS-0006). The authors also want to thank the Fédération INGE'LYSE for its financial support.

## 475 **References**

- 476 [1] E. Seeman, P.D. Delmas, Bone quality--the material and structural basis of bone strength  
477 and fragility., *N. Engl. J. Med.* 354 (2006) 2250–2261. doi:10.1056/NEJMra053077.
- 478 [2] J.Y. Rho, L. Kuhn-Spearing, P. Zioupos, Mechanical properties and the hierarchical  
479 structure of bone, *Med. Eng. Phys.* 20 (1998) 92–102. doi:10.1016/S1350-  
480 4533(98)00007-1.
- 481 [3] P. Dong, S. Hauptert, B. Hesse, M. Langer, P.J. Gouttenoire, V. Bousson, F. Peyrin, 3D  
482 osteocyte lacunar morphometric properties and distributions in human femoral cortical  
483 bone using synchrotron radiation micro-CT images, *Bone.* 60 (2014) 172–185.  
484 doi:10.1016/j.bone.2013.12.008.
- 485 [4] Y. Bala, E. Lefevre, J.P. Roux, C. Baron, P. Lasaygues, M. Pithioux, V. Kaftandjian, H. Follet,  
486 Pore network microarchitecture influences human cortical bone elasticity during growth  
487 and aging, *J. Mech. Behav. Biomed. Mater.* 63 (2016) 164–173.  
488 doi:10.1016/j.jmbbm.2016.05.018.
- 489 [5] G.E. Fantner, T. Hassenkam, J.H. Kindt, J.C. Weaver, H. Birkedal, L. Pechenik, J. a Cutroni, G.  
490 a G. Cidade, G.D. Stucky, D.E. Morse, P.K. Hansma, Sacrificial bonds and hidden length  
491 dissipate energy as mineralized fibrils separate during bone fracture., *Nat. Mater.* 4  
492 (2005) 612–616. doi:10.1038/nmat1428.
- 493 [6] R. Voide, P. Schneider, M. Stauber, P. Wyss, M. Stampanoni, U. Sennhauser, G.H. Van  
494 Lenthe, R. Müller, Time-lapsed assessment of microcrack initiation and propagation in  
495 murine cortical bone at submicrometer resolution, *Bone.* 45 (2009) 164–173.  
496 doi:10.1016/j.bone.2009.04.248.
- 497 [7] G.C. Reilly, Observations of microdamage around osteocyte lacunae in bone, *J. Biomech.*  
498 33 (2000) 1131–1134. doi:10.1016/S0021-9290(00)00090-7.
- 499 [8] D.B. Burr, M.B. Schaffler, R.G. Frederickson, Composition of the cement line and its  
500 possible mechanical role as a local interface in human compact bone., *J. Biomech.* 21  
501 (1988) 939–945. doi:10.1016/0021-9290(88)90132-7.
- 502 [9] Y.N. Yeni, C.U. Brown, Z. Wang, T.L. Norman, The influence of bone morphology on  
503 fracture toughness of the human femur and tibia, *Bone.* 21 (1997) 453–459.  
504 doi:10.1016/S8756-3282(97)00173-7.
- 505 [10] O.L. Katsamenis, T. Jenkins, P.J. Thurner, Toughness and damage susceptibility in human  
506 cortical bone is proportional to mechanical inhomogeneity at the osteonal-level, *Bone.* 76  
507 (2015) 158–168. doi:10.1016/j.bone.2015.03.020.
- 508 [11] U. Wolfram, J.J. Schwiedrzik, M.J. Mirzaali, A. Bürki, P. Varga, C. Olivier, F. Peyrin, P.K.  
509 Zysset, Characterizing microcrack orientation distribution functions in osteonal bone  
510 samples, *J. Microsc.* 00 (2016) 1–14. doi:10.1111/jmi.12440.
- 511 [12] R. Gauthier, M. Langer, H. Follet, C. Olivier, P.-J. Gouttenoire, L. Helfen, F. Rongi eras, D.  
512 Mitton, F. Peyrin, Influence of loading condition and anatomical location on human  
513 cortical bone linear micro-cracks, *J. Biomech.* (2019).  
514 doi:10.1016/j.jbiomech.2019.01.008.
- 515 [13] M. Granke, A.J. Makowski, S. Uppuganti, J.S. Nyman, Prevalent role of porosity and  
516 osteonal area over mineralization heterogeneity in the fracture toughness of human  
517 cortical bone, *J. Biomech.* 49 (2016) 2748–2755. doi:10.1016/j.jbiomech.2016.06.009.
- 518 [14] A. Bernhard, P. Milovanovic, E.A. Zimmermann, M. Hahn, D. Djonic, M. Krause, S. Breer, K.  
519 P uschel, M. Djuric, M. Amling, B. Busse, Micro-morphological properties of osteons reveal

- 520 changes in cortical bone stability during aging, osteoporosis, and bisphosphonate  
521 treatment in women, *Osteoporos. Int.* 24 (2013) 2671–2680. doi:10.1007/s00198-013-  
522 2374-x.
- 523 [15] R.F.M. van Oers, R. Ruimerman, E. Tanck, P.A.J. Hilbers, R. Huiskes, A unified theory for  
524 osteonal and hemi-osteonal remodeling, *Bone*. 42 (2008) 250–259.  
525 doi:10.1016/j.bone.2007.10.009.
- 526 [16] N.E. Lassen, T.L. Andersen, G.G. Pløen, K. Sjøe, E.M. Hauge, S. Harving, G.E.T. Eschen, J.M.  
527 Delaisse, Coupling of Bone Resorption and Formation in Real Time: New Knowledge  
528 Gained From Human Haversian BMUs, *J. Bone Miner. Res.* 32 (2017) 1395–1405.  
529 doi:10.1002/jbmr.3091.
- 530 [17] J.M. Delaisse, The reversal phase of the bone-remodeling cycle: cellular prerequisites for  
531 coupling resorption and formation, *Bonekey Rep.* 3 (2014) 1–8.  
532 doi:10.1038/bonekey.2014.56.
- 533 [18] A.M. Parfitt, Osteonal and hemi-osteonal remodeling: The spatial and temporal  
534 framework for signal traffic in adult human bone, *J. Cell. Biochem.* 55 (1994) 273–286.  
535 doi:10.1002/jcb.240550303.
- 536 [19] D.B. Burr, R.B. Martin, M.B. Schaffler, E.L. Radin, Bone remodeling in response to in vivo  
537 fatigue microdamage, *J. Biomech.* 18 (1985) 189–200. doi:10.1016/0021-  
538 9290(85)90204-0.
- 539 [20] V. Bentolila, T.M. Boyce, D.P. Fyhrie, R. Drumb, T.M. Skerry, M.B. Schaffler, Intracortical  
540 remodeling in adult rat long bones after fatigue loading, *Bone*. 23 (1998) 275–281.  
541 doi:10.1016/S8756-3282(98)00104-5.
- 542 [21] Y. Bala, D. Farlay, P.D. Delmas, P.J. Meunier, G. Boivin, Time sequence of secondary  
543 mineralization and microhardness in cortical and cancellous bone from ewes, *Bone*. 46  
544 (2010) 1204–1212. doi:10.1016/j.bone.2009.11.032.
- 545 [22] G. Boivin, D. Farlay, Y. Bala, A. Doublier, P.J. Meunier, P.D. Delmas, Influence of remodeling  
546 on the mineralization of bone tissue, *Osteoporos. Int.* 20 (2009) 1023–1026.  
547 doi:10.1007/s00198-009-0861-x.
- 548 [23] G. Boivin, P.J. Meunier, Changes in Bone Remodeling Rate Influence the Degree of  
549 Mineralization of Bone, *Connect. Tissue Res.* 43 (2002) 535–537.  
550 doi:10.1080/03008200290000934.
- 551 [24] P. Milovanovic, A. vom Scheidt, K. Mletzko, G. Sarau, K. Püschel, M. Djuric, M. Amling, S.  
552 Christiansen, B. Busse, Bone tissue aging affects mineralization of cement lines, *Bone*. 110  
553 (2018) 187–193. doi:10.1016/j.bone.2018.02.004.
- 554 [25] M. Langer, A. Pacureanu, H. Suhonen, Q. Grimal, P. Cloetens, F. Peyrin, X-Ray Phase  
555 Nanotomography Resolves the 3D Human Bone Ultrastructure, *PLoS One*. 7 (2012)  
556 e35691. doi:10.1371/journal.pone.0035691.
- 557 [26] M.T.K. Mulari, Q. Qu, P.L. Härkönen, H.K. Väänänen, Osteoblast-like cells complete  
558 osteoclastic bone resorption and form new mineralized bone matrix in vitro, *Calcif. Tissue*  
559 *Int.* 75 (2004) 253–261. doi:10.1007/s00223-004-0172-3.
- 560 [27] M.B. Schaffler, D.B. Burr, R.G. Frederickson, Morphology of the Osteonal Cement Line in  
561 Human-Bone, *Anat. Rec.* 217 (1987) 223–228.
- 562 [28] K. Raum, I. Leguerney, F. Chandelier, M. Talmant, A. Säed, F. Peyrin, P. Laugier, Site-

- 563 matched assessment of structural and tissue properties of cortical bone using scanning  
564 acoustic microscopy and synchrotron radiation  $\mu$ CT, *Phys. Med. Biol.* 51 (2006) 733–746.  
565 doi:10.1088/0031-9155/51/3/017.
- 566 [29] A. Ardizzoni, Osteocyte lacunar size-lamellar thickness relationships in human secondary  
567 osteons, *Bone*. 28 (2001) 215–219. doi:10.1016/S8756-3282(00)00417-8.
- 568 [30] K.M. Hannah, C.D.L. Thomas, J.G. Clement, F. De Carlo, A.G. Peele, Bimodal distribution of  
569 osteocyte lacunar size in the human femoral cortex as revealed by micro-CT, *Bone*. 47  
570 (2010) 866–871. doi:10.1016/j.bone.2010.07.025.
- 571 [31] J. Power, M. Doube, R.L. van Bezooijen, N. Loveridge, J. Reeve, Osteocyte recruitment  
572 declines as the osteon fills in: Interacting effects of osteocytic sclerostin and previous hip  
573 fracture on the size of cortical canals in the femoral neck, *Bone*. 50 (2012) 1107–1114.  
574 doi:10.1016/j.bone.2012.01.016.
- 575 [32] P. Varga, A. Pacureanu, M. Langer, H. Suhonen, B. Hesse, Q. Grimal, P. Cloetens, K. Raum, F.  
576 Peyrin, Investigation of the three-dimensional orientation of mineralized collagen fibrils  
577 in human lamellar bone using synchrotron X-ray phase nano-tomography, *Acta Biomater.*  
578 9 (2013) 8118–8127. doi:10.1016/j.actbio.2013.05.015.
- 579 [33] S. Schrof, P. Varga, L. Galvis, K. Raum, A. Masic, 3D Raman mapping of the collagen fibril  
580 orientation in human osteonal lamellae, *J. Struct. Biol.* 187 (2014) 266–275.  
581 doi:10.1016/j.jsb.2014.07.001.
- 582 [34] W. Wagermaier, H. S. Gupta, A. Gourrier, M. Burghammer, P. Roschger, P. Fratzl, Spiral  
583 twisting of fiber orientation inside bone lamellae, *Biointerphases*. 1 (2006) 1–5.  
584 doi:10.1116/1.2178386.
- 585 [35] A. Faingold, S.R. Cohen, N. Reznikov, H.D. Wagner, Osteonal lamellae elementary units:  
586 Lamellar microstructure, curvature and mechanical properties, *Acta Biomater.* 9 (2013)  
587 5956–5962. doi:10.1016/j.actbio.2012.11.032.
- 588 [36] H.S. Gupta, U. Stachewicz, W. Wagermaier, P. Roschger, H.D. Wagner, P. Fratzl, Mechanical  
589 modulation at the lamellar level in osteonal bone, *J. Mater. Res.* 21 (2006) 1913–1921.  
590 doi:10.1557/jmr.2006.0234.
- 591 [37] C. Ortiz, M. Dao, P. Vena, R. Contro, D. Carnelli, Orientation and size-dependent mechanical  
592 modulation within individual secondary osteons in cortical bone tissue, *J. R. Soc. Interface.*  
593 10 (2013) 20120953–20120953. doi:10.1098/rsif.2012.0953.
- 594 [38] J. Jowsey, M. Owen, J. Vaughan, Microradiographs and autoradiographs of cortical bone  
595 from monkeys injected with  $^{90}\text{Sr}$ , *Br. J. Exp. Pathol.* 34 (1953) 661–7.  
596 <http://www.ncbi.nlm.nih.gov/pubmed/13115599>.
- 597 [39] J. Jowsey, Studies of Haversian systems in man and some animals., *J. Anat.* 100 (1966)  
598 857–64. doi:10.1002/ajpa.
- 599 [40] G. Boivin, P.J. Meunier, The degree of mineralization of bone tissue measured by  
600 computerized quantitative contact microradiography, *Calcif. Tissue Int.* 70 (2002) 503–  
601 511. doi:10.1007/s00223-001-2048-0.
- 602 [41] Y.N. Yeni, T.L. Norman, Fracture toughness of human femoral neck: Effect of  
603 microstructure, composition, and age, *Bone*. 26 (2000) 499–504. doi:10.1016/S8756-  
604 3282(00)00258-1.
- 605 [42] J.G. Skedros, C.J. Kiser, K.E. Keenan, S.C. Thomas, Analysis of osteon morphotype scoring

- 606 schemes for interpreting load history: Evaluation in the chimpanzee femur, *J. Anat.* 218  
607 (2011) 480–499. doi:10.1111/j.1469-7580.2011.01348.x.
- 608 [43] R. Gauthier, M. Langer, H. Follet, C. Olivier, P.-J. Gouttenoire, L. Helfen, F. Rongi eras, D.  
609 Mitton, F. Peyrin, 3D micro structural analysis of human cortical bone in paired femoral  
610 diaphysis, femoral neck and radial diaphysis, *J. Struct. Biol.* 204 (2018) 182–190.  
611 doi:10.1016/j.jsb.2018.08.006.
- 612 [44] V. Bousson, F. Peyrin, C. Bergot, M. Hausard, A. Sautet, J.-D. Laredo, Cortical bone in the  
613 human femoral neck: three-dimensional appearance and porosity using synchrotron  
614 radiation., *J. Bone Miner. Res.* 19 (2004) 794–801. doi:10.1359/JBMR.040124.
- 615 [45] Z. Peter, V. Bousson, C. Bergot, F. Peyrin, A constrained region growing approach based on  
616 watershed for the segmentation of low contrast structures in bone micro-CT images,  
617 *Pattern Recognit.* 41 (2008) 2358–2368. doi:10.1016/j.patcog.2007.12.011.
- 618 [46] D.M.L. Cooper, B. Erickson, A.G. Peele, K. Hannah, C.D.L. Thomas, J.G. Clement,  
619 Visualization of 3D osteon morphology by synchrotron radiation micro-CT, *J. Anat.* 219  
620 (2011) 481–489. doi:10.1111/j.1469-7580.2011.01398.x.
- 621 [47] Q. Vallet, N. Bochud, C. Chappard, P. Laugier, J.-G. Minonzio, In Vivo Characterization of  
622 Cortical Bone Using Guided Waves Measured by Axial Transmission, *IEEE Trans. Ultrason.*  
623 *Ferroelectr. Freq. Control.* 63 (2016) 1361–1371. doi:10.1109/TUFFC.2016.2587079.
- 624 [48] B. Burt-Pichat, H. Follet, G. Toulemonde, M. Arlot, P. Delmas, R. Chapurlat, Methodological  
625 approach for the detection of both microdamage and fluorochrome labels in ewe bone  
626 and human trabecular bone, *J. Bone Miner. Metab.* 29 (2011) 756–764.  
627 doi:10.1007/s00774-011-0291-7.
- 628 [49] D. Paganin, S.C. Mayo, T.E. Gureyev, P.R. Miller, S.W. Wilkins, Simultaneous phase and  
629 amplitude extraction from a single defocused image of a homogeneous object, *J. Microsc.*  
630 206 (2002) 33–40. doi:10.1046/j.1365-2818.2002.01010.x.
- 631 [50] I.S. Maggiano, C.M. Maggiano, J.G. Clement, C.D.L. Thomas, Y. Carter, D.M.L. Cooper, Three-  
632 dimensional reconstruction of Haversian systems in human cortical bone using  
633 synchrotron radiation-based micro-CT: morphology and quantification of branching and  
634 transverse connections across age, *J. Anat.* 228 (2016) 719–732. doi:10.1111/joa.12430.
- 635 [51] K. Schladitz, J. Ohser, W. Nagel, Measuring Intrinsic Volumes in Digital 3d Images, *Discret.*  
636 *Geom. Comput. Imag.* 4245 (2006) 247–258. doi:10.1007/11907350\_21.
- 637 [52] D.W. Dempster, J.E. Compston, M.K. Drezner, F.H. Glorieux, J.A. Kanis, H. Malluche, P.J.  
638 Meunier, S.M. Ott, R.R. Recker, A.M. Parfitt, Standardized nomenclature, symbols, and  
639 units for bone histomorphometry: A 2012 update of the report of the ASBMR  
640 Histomorphometry Nomenclature Committee, *J. Bone Miner. Res.* 28 (2013) 2–17.  
641 doi:10.1002/jbmr.1805.
- 642 [53] M.A. Parfitt, M.K. Drezner, F.H. Glorieux, J. a Kanis, H. Malluche, P.J. Meunier, S.M. Ott, R.R.  
643 Recker, Bone Histomorphometry : Standardization of Nomenclature, Symbols, and Units,  
644 2 (1987) 595–610.
- 645 [54] E. Mart n-Badosa, A. Elmoutaouakkil, S. Nuzzo, D. Amblard, L. Vico, F. Peyrin, A method for  
646 the automatic characterization of bone architecture in 3D mice microtomographic images,  
647 *Comput. Med. Imaging Graph.* 27 (2003) 447–458. doi:10.1016/S0895-6111(03)00031-4.
- 648 [55] J.G. Skedros, J.L. Holmes, E.G. Vajda, R.D. Bloebaum, Cement lines of secondary osteons in  
649 human bone are not mineral-deficient: New data in a historical perspective, *Anat. Rec.* -

- 650 Part A Discov. Mol. Cell. Evol. Biol. 286 (2005) 781–803. doi:10.1002/ar.a.20214.
- 651 [56] A.G. Robling, S.D. Stout, Morphology of the Drifting Osteon, *Cells Tissues Organs*. 164  
652 (1999) 192–204. doi:10.1159/000016659.
- 653 [57] P. Atkinson, A. Hallsworth, The spatial structure of bone, in: R. Harrison, V. Navaratnam  
654 (Eds.), *Prog. Anat.*, Cambridge University Press, Cambridge, 1982: pp. 179–99.
- 655 [58] G. Marotti, M.A. Muglia, C. Palumbo, Collagen texture and osteocyte distribution in  
656 lamellar bone., *Ital. J. Anat. Embryol.* 100 Suppl (1995) 95–102.
- 657 [59] L.F. Bonewald, The amazing osteocyte, *J. Bone Miner. Res.* 26 (2011) 229–238.  
658 doi:10.1002/jbmr.320.
- 659 [60] T.A. Franz-Odenaal, B.K. Hall, P.E. Witten, Buried alive: How osteoblasts become  
660 osteocytes, *Dev. Dyn.* 235 (2006) 176–190. doi:10.1002/dvdy.20603.
- 661 [61] P.R. Buenzli, P. Pivonka, D.W. Smith, Bone refilling in cortical basic multicellular units:  
662 Insights into tetracycline double labelling from a computational model, *Biomech. Model.*  
663 *Mechanobiol.* 13 (2014) 185–203. doi:10.1007/s10237-013-0495-y.
- 664 [62] P.R. Buenzli, Osteocytes as a record of bone formation dynamics: A mathematical model of  
665 osteocyte generation in bone matrix, *J. Theor. Biol.* 364 (2015) 418–427.  
666 doi:10.1016/j.jtbi.2014.09.028.
- 667 [63] G. Marotti, A.Z. Zallone, M. Ledda, Number, size and arrangement of osteoblasts in osteons  
668 at different stages of formation, *Calcif. Tissue Res.* 21 (1975) 96–101.  
669 doi:10.1007/BF02546434.
- 670 [64] M.A. Alias, P.R. Buenzli, Osteoblasts infill irregular pores under curvature and porosity  
671 controls: a hypothesis-testing analysis of cell behaviours, *Biomech. Model. Mechanobiol.*  
672 17 (2018) 1357–1371. doi:10.1007/s10237-018-1031-x.
- 673 [65] M. McKee, A. Nanci, Osteopontin and the Bone Remodeling Sequence, *Ann NY Acad Sci.*  
674 760 (1995) 177–189. doi:10.1111/j.1749-6632.1995.tb44629.x.
- 675 [66] F. Repp, P. Kollmannsberger, A. Roschger, M. Kerschnitzki, A. Berzlanovich, G. Gruber, P.  
676 Roschger, W. Wagermaier, R. Weinkamer, Spatial heterogeneity in the canalicular density  
677 of the osteocyte network in human osteons, *Bone Reports.* 6 (2017) 101–108.  
678 doi:10.1016/j.bonr.2017.03.001.
- 679 [67] B. Hesse, P. Varga, M. Langer, A. Pacureanu, S. Schrof, N. Männicke, H. Suhonen, P. Maurer,  
680 P. Cloetens, F. Peyrin, K. Raum, Canalicular Network Morphology Is the Major  
681 Determinant of the Spatial Distribution of Mass Density in Human Bone Tissue: Evidence  
682 by Means of Synchrotron Radiation Phase-Contrast nano-CT, *J. Bone Miner. Res.* 30  
683 (2015) 346–356. doi:10.1002/jbmr.2324.
- 684 [68] K. Hoshi, S. Kawamoto, S. Ejiri, H. Ozawa, K. Tazawa, M. Tanaka, Osteocytic osteolysis  
685 observed in rats to which parathyroid hormone was continuously administered, *J. Bone*  
686 *Miner. Metab.* 22 (2004) 524–529. doi:10.1007/s00774-004-0519-x.
- 687 [69] M. Prideaux, C. Schutz, A.R. Wijenayaka, D.M. Findlay, D.G. Campbell, L.B. Solomon, G.J.  
688 Atkins, Isolation of osteocytes from human trabecular bone, *Bone.* 88 (2016) 64–72.  
689 doi:10.1016/j.bone.2016.04.017.
- 690 [70] R.T. Ormsby, L.B. Solomon, D.M. Findlay, G.J. Atkins, M. Cantley, D.R. Haynes, M. Kogawa,  
691 Evidence that osteocyte perilacunar remodelling contributes to polyethylene wear

- 692 particle induced osteolysis, *Acta Biomater.* 33 (2016) 242–251.  
693 doi:10.1016/j.actbio.2016.01.016.
- 694 [71] H. Qing, L.F. Bonewald, Osteocyte remodeling of the perilacunar and pericanalicular  
695 matrix., *Int. J. Oral Sci.* 1 (2009) 59–65. doi:10.4248/ijos.09019.
- 696 [72] A. Roschger, P. Roschger, W. Wagermaier, J. Chen, A. van Tol, F. Repp, S. Blouin, A.  
697 Berzlanovich, G.M. Gruber, K. Klaushofer, P. Fratzl, R. Weinkamer, The contribution of the  
698 pericanalicular matrix to mineral content in human osteonal bone, *Bone.* (2019)  
699 #pagerange#. doi:10.1016/j.bone.2019.03.018.
- 700 [73] E.A. Zimmermann, C. Riedel, F. Schmidt, K. Stockhausen, Y. Chushkin, E. Schaible, B.  
701 Gludovatz, E. Vettorazzi, F. Zontone, K. Püschel, M. Amling, R. Ritchie, B. Busse, Mechanical  
702 competence and bone quality develop during skeletal growth, *J. Bone Miner. Res.* (2019)  
703 0–3. doi:10.1002/jbmr.3730.
- 704 [74] M.B. Schaffler, K. Choi, C. Milgrom, Aging and matrix microdamage accumulation in human  
705 compact bone, *Bone.* 17 (1995) 521–525. doi:10.1016/8756-3282(95)00370-3.
- 706 [75] F.J. O'Brien, D. Taylor, T.C. Lee, The effect of bone microstructure on the initiation and  
707 growth of microcracks, 2005. doi:10.1016/j.orthres.2004.08.005.
- 708 [76] N.J. Wachter, P. Augat, G.D. Krischak, M. Mentzel, L. Kinzl, L. Claes, Prediction of cortical  
709 bone porosity in vitro by microcomputed tomography., *Calcif. Tissue Int.* 68 (2001) 38–  
710 42. doi:10.1007/s002230001182.
- 711 [77] a. a. Griffith, The Phenomena of Rupture and Flow in Solids, *Philos. Trans. R. Soc. A Math.*  
712 *Phys. Eng. Sci.* 221 (1921) 163–198. doi:10.1098/rsta.1921.0006.
- 713 [78] V. Canè, G. Marotti, G. Volpi, D. Zaffe, S. Palazzini, F. Remaggi, M.A. Muglia, Size and density  
714 of osteocyte lacunae in different regions of long bones, *Calcif. Tissue Int.* 34 (1982) 558–  
715 563. doi:10.1007/BF02411304.
- 716 [79] H. Chen, X. Zhou, S. Shoumura, S. Emura, Y. Bunai, Age- And gender-dependent changes in  
717 three-dimensional microstructure of cortical and trabecular bone at the human femoral  
718 neck, *Osteoporos. Int.* 21 (2010) 627–636. doi:10.1007/s00198-009-0993-z.
- 719 [80] A.J. Burghardt, G.J. Kazakia, S. Ramachandran, T.M. Link, S. Majumdar, Age- and gender-  
720 related differences in the geometric properties and biomechanical significance of  
721 intracortical porosity in the distal radius and tibia., *J. Bone Miner. Res.* 25 (2010) 983–  
722 993. doi:10.1359/jbmr.091104.
- 723 [81] B. Busse, D. Djonc, P. Milovanovic, M. Hahn, K. Püschel, R.O. Ritchie, M. Djuric, M. Amling,  
724 Decrease in the osteocyte lacunar density accompanied by hypermineralized lacunar  
725 occlusion reveals failure and delay of remodeling in aged human bone, *Aging Cell.* 9  
726 (2010) 1065–1075. doi:10.1111/j.1474-9726.2010.00633.x.

727